Chapter 5

Nucleation and growth of antiferrodistorted Polar nano regions into a long-range ferroelectric matrix in a Sodium Niobate-based complex relaxor

5.1 Introduction

Relaxor Ferroelectrics (RFs) have consistently drawn attention of the scientific community due to their thermal stability and suitability for a wide range of applications, *viz.,* multilayered ceramic capacitors, sensors, high-precision actuators etc. [120, 122, 125, 270, 295]. Relaxor ferroelectrics are primarily characterized by two features: (i) diffuse dielectric permittivity (ε') around the maximum, and (ii) strong frequency dependence of temperature corresponding to dielectric maximum (T_m) [18, 46, 135]. Relaxor behaviour in perovskite based (ABO_3) dielectric materials can be induced by substitution disorder at cationic sites, causing local random electric and/or elastic fields due to local charge imbalance

and/or ionic radius mismatch, e.g $Pb(Mg_{1/3}Nb_{2/3})O_3$, $Pb(Sc_{1/2}Ta_{1/2})O_3$, $Ba(Ti_{1-x}Zr_x)O_3$, $Ba(Ti_{1-x}Sn_x)O_3$, $(K_{1-x}Li_x)TaO_3$ etc. [71, 120, 261, 270, 296, 297, 298, 299].

At high temperatures, relaxors remain in a non-polar paraelectric phase, similar to the paraelectric phase of conventional ferroelectrics [140, 255, 270, 300, 301]. As the temperature decreases, they transform into an ergodic relaxor state [120]. In this state, nanoscale heterogeneities, known as Polar Nano Regions (PNRs), nucleate and start to grow. These PNRs appear below Burns Temperature (T_B) and play a crucial role in tuning physical properties of relaxor ferroelectrics [120, 130, 302, 303]. Immediately below T_B, there exists a short-lived correlation among PNRs, resulting in a zero time-averaged polarization. Upon further cooling, an intermediate temperature T* has been reported in relaxor ferroelectrics [132, 133, 134]. It is believed that below T*, interaction among Polar Nano Regions (PNRs) gradually enhances, and the system starts transforming into a static state from a dynamic state. [130]. On further decreasing temperatures, relaxors eventually evolve into a glass-like structure below Vogel-Fulcher freezing temperature (T_{VF}) [130]. The state of relaxors below T_{VF} is referred to as non-ergodic [148, 304].

In contrast to conventional ferroelectrics, canonical relaxors do not exhibit a long-range ferroelectric phase below the temperature corresponding to the dielectric maximum [135]. However, a long-range ferroelectric ordering can be stabilized in canonical relaxors at low temperatures (below T_{VF}) on the application of an external electric field [136]. On the other hand, there are reports where long-range ferroelectric ordering can be stabilized solely by lowering the temperature below the Vogel–Fulcher freezing (T_{VF}) [137, 138, 139, 140, 141]. Based on the ordering below T_{VF}, relaxors can be classified into two categories. The first category include relaxors exhibiting a long-range ferroelectric order below T_{VF} (e.g. $PbMg_{1/3}Nb_{2/3}O_3$-x$PbTiO_3$ (PMN-PT))[140] while the second category do not experience a ferroelectric phase transition even at the cryogenic temperatures (e.g. $PbMg_{1/3}Nb_{2/3}O_3$ (PMN)) [142, 143]. To explain the above-mentioned relaxor to

ferroelectric phase transition in relaxors, various models have been proposed [137, 138]. Chu et al. used a description based on the bond strength of B-site cation to explain the ferroelectric phase transition in relaxors [137]. On the other hand, Dai et al. described the thermally driven relaxor to normal ferroelectric phase transition within a thermodynamic framework [138].

For decades, lead-based relaxor materials have been in vogue, but concerns over the toxic effects of lead on human health led researchers to explore lead-free alternatives that can provide similar properties [122]. In chapter 3, we reported a lead-free solid solution of $NaNbO_3$ (NN) and $Ba_{0.9}Ca_{0.1}TiO_3$ (BCT), where 0.75 $NaNbO_3$- 0.25 $(Ba_{0.9}Ca_{0.1})TiO_3$ (NN-25BCT) demonstrates relaxor behaviour [71]. In the present chapter, we will discuss the temperature evolution of short, medium, and long-range crystal structure of NN-25BCT in a temperature range 110 K $\leq$ T $\leq$ 500 K. Dielectric analysis demonstrates nucleation and growth of polar nano-regions (PNRs) below the Burns temperature (T $\leq$ T_B). Synchrotron X-ray diffraction (SXRD) data clearly reveal the relaxor to ferroelectric phase transition in NN-25BCT below T_{VF}. Distortion mode analysis of the low-temperature ferroelectric phase (SG: *P4bm*) provides experimental evidence of competitive interactions between ferroelectricity and in-phase octahedral rotations. Raman spectroscopy, Pair Distribution function analysis, in conjunction with SXRD data refinements, suggest the presence of local polar order with tetragonal symmetry for T > T_{VF} in the long-range paraelectric matrix.

5.2 Experimental

Samples with nominal composition 0.75 $NaNbO_3$–0.25 $Ba_{0.9}Ca_{0.1}TiO_3$ (NN-25BCT) were synthesized via the conventional solid-state reaction route (see experimental section of Chapter 3 for more details). The Synchrotron X-ray Diffraction and PDF (Pair Distribution Function) data were collected using Beamline 28-ID-2 (X-ray Powder Diffraction, XPD)

at NSLS2 (National Synchrotron Light Source), at Brookhaven National Laboratory, with a wavelength of 0.18210 Å. High-Q measurements were conducted with a maximum instrumental Q value (Q_{max}) of 25 $^{-1}$. Additionally, high-Q data for an empty borosilicate capillary were collected for background subtraction, which is necessary for converting the raw diffraction data into the total scattering structure function S(Q). The S(Q) was obtained from high-Q (Q_{max} = 25 Å^{-1}) SXRD data after performing standard normalization and background corrections on the raw scattering data using the PDFgetX3 program [224]. To obtain the corresponding reduced PDFs, the S(Q) data were then Fourier-transformed using the function

$$G(r) = (2/\pi) \int_{Q_{\min}}^{Q_{\max}} Q[S(Q) - 1] \sin(Qr)\, dQ$$

where Q_{max} = 25 Å^{-1} and Q_{min} = 0.6291 Å^{-1}. The structural refinements of the experimental atomic PDFs were carried out using the PDFgui program [225].

Silver electrodes were fired on the top and bottom surfaces of the samples for the electrical measurements. The dielectric measurements were carried out using a Keysight LCR meter in the temperature range of 100 K - 550 K. A precision LC II ferroelectric tester (Radiant Technologies Inc.) was used to obtain the polarization vs. electric field (P-E) hysteresis loops and associated current vs. electric field loops (I-E). Raman measurements were performed using a Horiba LabRAM HR spectrometer equipped with an Olympus BX41 microscope. An excitation wavelength of 514.5 nm from a Lexel Model-95 argon ion laser was used. Variable-temperature Raman spectra were collected by placing the samples in a Linkam THMS600 temperature-controlled microscope stage. The laser beam was focused onto the sample surface using a 50x LWD objective lens (numerical aperture = 0.50), and the backscattered signal was dispersed using a 600 lines/mm grating and detected with a liquid nitrogen-cooled CCD. Data acquisition was carried out using LabSpec v5 software. The laser power at the sample surface was maintained at approximately 0.4 mW, and care

was taken to ensure the absence of any laser-induced local heating effects. All Raman spectra were corrected using the Bose-Einstein temperature factor as follows:

$$I_c(\tilde{\nu}) = \frac{I_m(\tilde{\nu})}{n(\tilde{\nu},T)+1} \quad \text{where} \quad n(\tilde{\nu},T) = \frac{1}{\exp\left(\frac{hc\tilde{\nu}}{kT}\right)-1}$$

Here, $I_c(\tilde{\nu})$ is the corrected Raman intensity, $I_m(\tilde{\nu})$ is the measured intensity, and $n(\tilde{\nu},T)$ is the Bose–Einstein thermal population factor, with $\tilde{\nu}$ representing the wavenumber. Further, Raman spectra were deconvoluted and fitted using the Lorentzian function.

5.3 Results And Discussion

5.3.1 Long-range structural analysis

In Chapter 3, we examined composition-dependent phase transitions of (1-x) $NaNbO_3$-x $Ba_{0.9}Ca_{0.1}TiO_3$ (NN-xBCT) for $0.00 \leq x \leq 1.00$ [71]. We observed a relaxor ferroelectric-like behaviour for $x = 0.25$, characterised by a high diffusion coefficient ($\gamma = 1.94$). Fig. 5.1(a) illustrates temperature-dependent real (ε') and imaginary (ε'') parts of dielectric permittivity at various frequencies (1 KHz - 1 MHz) in the temperature range $100 \leq T \leq 550$ K. The real part of dielectric permittivity exhibits a diffuse nature around the maximum ($T_m \approx 285$ K) and demonstrates a typical relaxor behaviour. This relaxor behaviour can be attributed to the presence of multiple cations with different oxidation states/sizes occupying the same crystallographic site, resulting in local strain and local fields simultaneously. Fig. 5.1(c) shows the inverse of dielectric permittivity ($1/\varepsilon'$) as a function of temperature at 10 kHz. For NN-25BCT, the dielectric permittivity deviates from the Curie-Weiss law above T_m (≈ 285 K). However, $1/\varepsilon'$ exhibits linear behaviour above $T \approx 410$ K. The temperature at which the deviation occurs is referred to as the Burns temperature (T_B). This temperature (T_B) marks the onset of nucleation and growth of polar nano regions

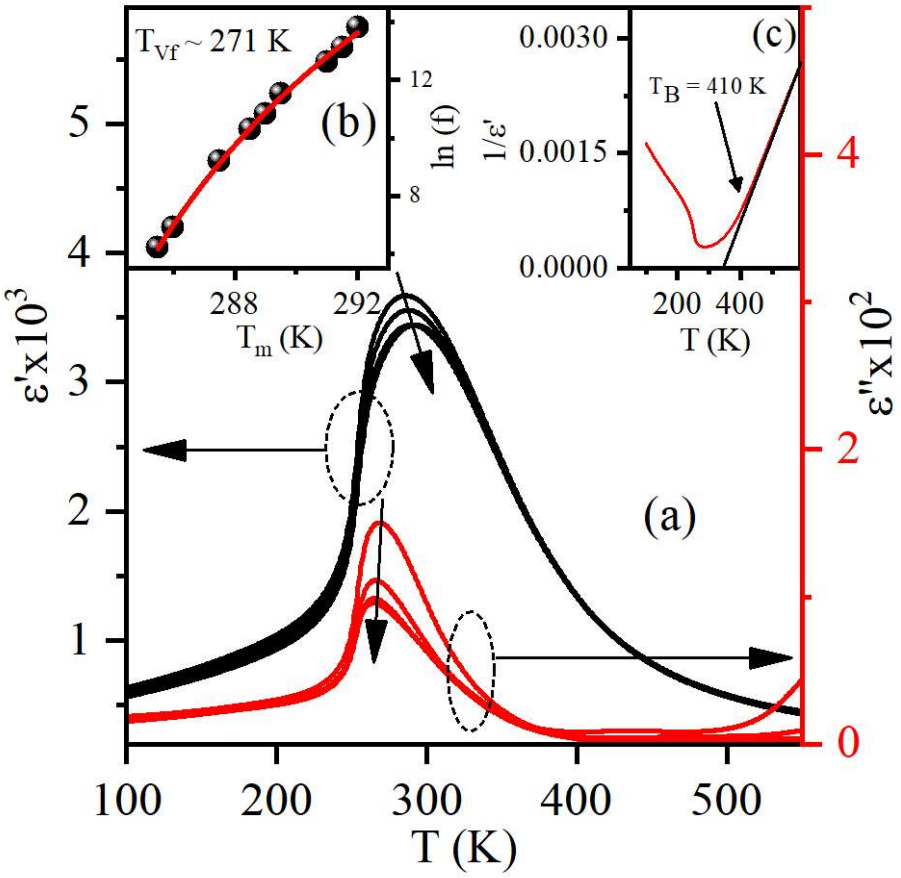

Fig. 5.1 (a) Temperature-dependent evolution of real and imaginary part of dielectric permittivity.(b) Vogel-Flucher fitting of the temperatures corresponding to the dielectric to estimate the freezing temperature. (c) The inverse of dielectric permittivity as a function of temperature marks the Burns Temperature.

(PNRs) that become more pronounced as the temperature decreases. At high temperatures (but below T_B), these PNRs are mobile, and their dynamics slow down on cooling. The PNRs freeze in a glass-like state below a temperature ($T = T_{VF}$), which can be determined using the Vogel-Fulcher (V-F) relation.

$$f = f_0 \exp\left[-\frac{E_a}{k(T_{\max} - T_{VF})}\right] \tag{5.1}$$

where T_{VF} is the static freezing temperature, E_a is the activation energy, f_o is an attempt frequency, and T_{max} is the temperature of the dielectric permittivity maximum [149, 305].

Fig. 5.1(b) shows Vogel-Fulcher fitting of the real part of the permittivity of NN-25BCT in the frequency range of 500 Hz to 1 MHz. The data were well-fitted by the Vogel-Fulcher equation with pre-exponential factor f_o = 7.68 x 10^{12} Hz, activation energy E_a = 0.028 eV, and Vogel-Fulcher freezing temperature $T_{VF} \approx 271$ K, respectively. These values closely align with those reported on similar materials [122, 306]. Moreover, it has been reported earlier that relaxors with activation energy close to the present value transform into a long-range ferroelectric phase at low temperatures [137]. Therefore, we aim to explore relaxor-to-ferroelectric phase transition below freezing temperature T_{VF} (if any).

To explore temperature-dependent structural phase transitions of NN-25BCT, we have performed Synchrotron X-ray diffraction measurements. The indexing of the diffraction pattern has been done with respect to a doubled perovskite cell (dpc). Fig.5.2(b)-(d) depicts main perovskite reflections *viz.,* $\{400\}_{dpc}$, $\{440\}_{dpc}$, and $\{444\}_{dpc}$ for a temperature range $110 \leq T \leq 500$ K. Fig.5.2(a) demonstrates the appearance of the superlattice reflection(s) on decreasing temperature below 400 K.

At 500 K, all the reflections are singlet in nature: a typical feature of high-temperature phase in relaxors having a cubic structure with $Pm\bar{3}m$ space group [138, 307]. At low temperatures, a weak shoulder appears near $\{400\}_{dpc}$ at a lower 2θ and $\{440\}_{dpc}$ becomes asymmetric. Moreover, we see the appearance of a weak superlattice reflection near $\{222\}_{dpc}$ reflection for $T \leq 400$. This weak reflection was indexed as $\{310\}$ with respect to the doubled perovskite cell and is associated with in-phase octahedral rotation [119]. The superlattice reflection remains stable down to the lowest studied temperature, i.e., 110 K. The main perovskite reflections, *viz.,* $\{h00\}_{dpc}$ and $\{hh0\}_{dpc}$ split into two peaks, whereas $\{hhh\}_{dpc}$ reflections remain singlet, suggesting a tetragonal symmetry. Such splitting of main perovskite reflections has been observed in pure $NaNbO_3$ at high temperatures [SG: *P4/mbm* (paraelectric); tilt system: $a_0^0a_0^0c_0^+$] and $BaTiO_3$ at ambient conditions [SG: *P4mm* (ferroelectric)] [36]. However, the presence of superlattice reflections along with splitting in

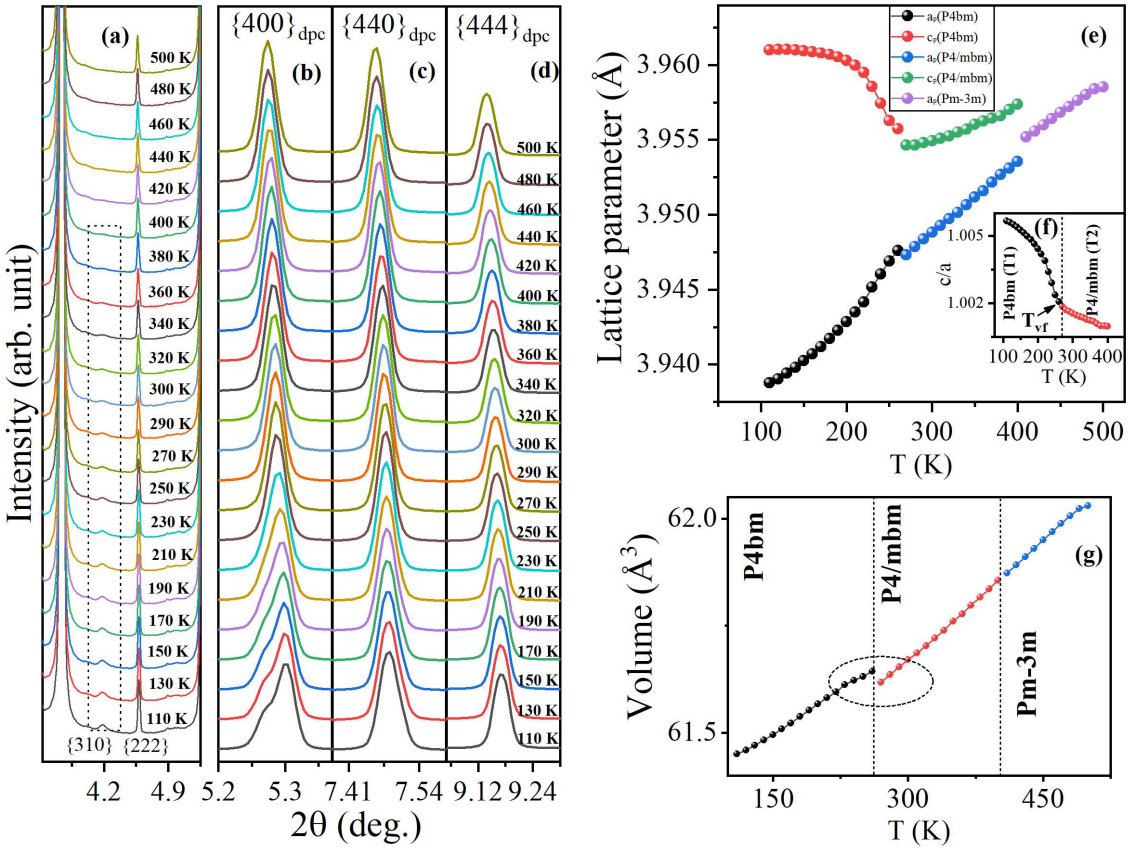

Fig. 5.2 Temperature-dependent evolution of (a) superlattice reflections, (b)-(d) main perovskite reflections. Evolution of (e) lattice parameters, (g) volume of the elementary cell, and (f) tetragonality of the elementary cell as a function of temperature.

the main perovskite reflections of NN-25BCT discards the Barium Titanate-like tetragonal phase (SG: *P4mm*), which results only due to octahedral distortion. Following the literature on similar systems, a plausible ferroelectric tetragonal phase with in-phase octahedral rotations is *P4bm* space group(tilt system: $a_0^0 a_0^0 c_+^+$, cell size: $\sqrt{2}a_p \times \sqrt{2}a_p \times c_p$) which can be visualized as a 'polar version' of the tilt orientated tetragonal phase observed in the paraelectric region of $NaNbO_3$ [36, 119, 308]. The presence of a superlattice reflection (due to an in-phase octahedral tilt) and splitting of the main perovskite reflections suggests a paraelectric tetragonal phase with a *P4/mbm* (T1) space group at ambient conditions. Nonetheless, a ferroelectric tetragonal model (SG: *P4bm* (T2)) is plausible below the V-F freezing temperature, i.e., $T_{VF} \approx 270$ K. To confirm the evolution of the crystallographic

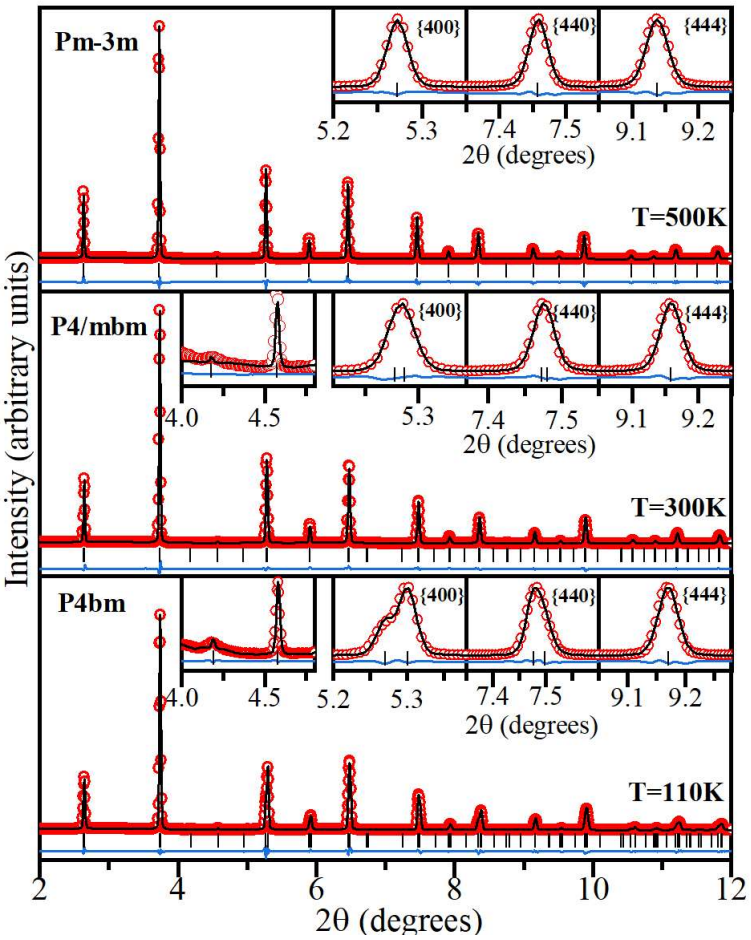

Fig. 5.3 Rietveld Refinement fit of the diffraction pattern at 500 K, 300 K, and 110 K using the $Pm\bar{3}m$, *P4/mbm*, *P4bm* space group, respectively. The inset shows the fitting around the main perovskite peaks and superlattice reflections.

structures as a function of temperature, Rietveld refinements of the diffraction patterns have been carried out using the FULLPROF package [214]. We have used the following models to fix the diffraction patterns **(i)** $Pm\bar{3}m$ (PE) [410$\leq$ T$\leq$500 K] **(ii)** *P4/mbm* (PE) [270$\leq$ T$\leq$400 K] **(iii)** *P4bm* (FE) [110$\leq$T$\leq$260 K]. The choice of these models has been made on the basis of splitting in main perovskite reflections, the appearance of superlattice reflections, and following the literature on similar materials. Fig. 5.2(e) shows the evolution of reduced lattice parameters as a function of temperature. The transition from a centrosymmetric tetragonal phase with *P4/mbm* space group (paraelectric) to a non-centrosymmetric tetragonal phase with *P4bm* space group (ferroelectric) is evident

Table 5.1 Structural parameters and agreement factors for NN-25BCT obtained from the Rietveld refinements of the Synchrotron X-ray diffraction pattern at various temperatures using *P4bm* model.

Space group: P4bm(110 K)					Space group: P4bm(130 K)			
Atoms	*x*	*y*	*z*	U_{eq}(Å^2)	*x*	*y*	*z*	U_{eq}(Å^2)
Na/Ba/Ca	0.000	0.500	0.493(7)	0.0065(11)	0.000	0.500	0.492(3)	0.0064(6)
Nb/Ti	0.000	0.000	0.000	0.0068(6)	0.000	0.000	0.000	0.0069(3)
O1	0.000	0.000	0.52(2)	0.016(9)	0.000	0.000	0.52(2)	0.017(7)
O2	0.263(5)	0.237(5)	0.044(6)	0.010(5)	0.262(3)	0.238(3)	0.044(6)	0.009(4)
a=*b*=5.5695(3)Å, *c*=3.9610(3)Å					*a*=*b*=5.5704(3)Å, *c*=3.9610(2)Å			
V= 122.87(1) Å^3, R_{wp}=2.85, R_{bragg}=1.71					*V*= 122.91(1) Å^3, R_{wp}=2.83, R_{bragg}=1.63			
Space group: *P4bm*(150 K)					Space group: *P4bm*(170 K)			
Atoms	*x*	*y*	*z*	U_{eq}(Å^2)	*x*	*y*	*z*	U_{eq}(Å^2)
Na/Ba/Ca	0.000	0.500	0.490(3)	0.0064(6)	0.000	0.500	0.489(3)	0.0065(6)
Nb/Ti	0.000	0.000	0.000	0.0070(3)	0.000	0.000	0.000	0.0071(3)
O1	0.000	0.000	0.52(2)	0.019(7)	0.000	0.000	0.52(2)	0.018(7)
O2	0.262(3)	0.238(3)	0.043(6)	0.008(4)	0.262(3)	0.238(3)	0.041(5)	0.009(4)
a=*b*=5.5716(3)Å, *c*=3.9609(2)Å					*a*=*b*=5.5730(3)Å, *c*=3.9607(2)Å			
V= 122.96(1) Å^3, R_{wp}=2.75 , R_{bragg}=1.67					*V*= 123.01(1) Å^3, R_{wp}=2.70, R_{bragg}=1.72			
Space group: *P4bm*(190 K)					Space group: *P4bm*(210 K)			
Atoms	*x*	*y*	*z*	U_{eq}(Å^2)	*x*	*y*	*z*	U_{eq}(Å^2)
Na/Ba/Ca	0.000	0.500	0.488(3)	0.0065(7)	0.000	0.500	0.487(3)	0.0066(7)
Nb/Ti	0.000	0.000	0.000	0.0073(4)	0.000	0.000	0.000	0.0075(4)
O1	0.000	0.000	0.51(2)	0.018(8)	0.000	0.000	0.51(3)	0.018(8)
O2	0.262(3)	0.238(3)	0.040(5)	0.009(4)	0.262(4)	0.238(4)	0.038(6)	0.009(4)
a=*b*=5.5745(3) Å, *c*=3.9605(2)Å					*a*=*b*=5.5762(2)Å, *c*=3.9599(2)Å			
V= 123.07(1) Å^3, R_{wp}=2.70, R_{bragg}=1.84					*V*= 123.13(1) Å^3, R_{wp}=2.74, R_{bragg}=1.99			
Space group: *P4bm*(230 K)					Space group: *P4bm*(250 K)			
Atoms	*x*	*y*	*z*	U_{eq}(Å^2)	*x*	*y*	*z*	U_{eq}(Å^2)
Na/Ba/Ca	0.000	0.500	0.486(2)	0.0065(7)	0.000	0.500	0.485(2)	0.0066(7)
Nb/Ti	0.000	0.000	0.000	0.0079(4)	0.000	0.000	0.000	0.0079(4)
O1	0.000	0.000	0.50(3)	0.017(9)	0.000	0.000	0.49(3)	0.016(12)
O2	0.261(3)	0.239(3)	0.038(6)	0.009(5)	0.260(4)	0.240(4)	0.038(5)	0.009(7)
a=*b*=5.5786(2)Å, *c*=3.9585(3)Å					*a*=*b*=5.5810(3)Å, *c*=3.9562(3)Å			
V= 123.19(1) Å^3, R_{wp}=2.87, R_{bragg}=2.19					*V*= 123.23(1) Å^3, R_{wp}=3.29, R_{bragg}=2.44			

from a discontinuity in the unit cell volume and a non-analytical behaviour in tetragonality around T $\approx$ 270 K. This temperature coincides with the V-F freezing temperature T_{VF} $\approx$ 270 K (see Fig. 5.2 (f) & 5.2 (g)). Similar characteristics of the phase transitions are also observed for PMN-PT, PZN, etc., where relaxors undergo a long-range ferroelectric phase transition below Vogel-Fulcher freezing temperature (T_{VF})[137, 138, 139, 140, 141]. Fig. 5.3 depicts the fitted diffraction patterns of NN-25BCT for some representative temperatures. Tables 5.1, 5.2, and 5.3 present the lattice parameters, atomic coordinates, thermal parameters, and goodness of fit parameter (R_{wp}) obtained after refinements of the diffraction patterns collected at various temperatures. Henceforth, Rietveld refinements, along with reasonable agreement factors, suggest a long-range ferroelectric order below the

Table 5.2 Structural parameters and agreement factors for NN-25BCT obtained from the Rietveld refinements of the Synchrotron X-ray diffraction pattern at various temperatures using *P4/mbm* model.

Space group: *P4/mbm*(270 K)					Space group: *P4/mbm*(290 K)			
Atoms	*x*	*y*	*z*	U_{eq}(Å^2)	*x*	*y*	*z*	U_{eq}(Å^2)
Na/Ba/Ca	0.000	0.500	0.500	0.0089(6)	0.000	0.500	0.500	0.0100(7)
Nb/Ti	0.000	0.000	0.000	0.0090(3))	0.000	0.000	0.000	0.0086(4)
O1	0.000	0.000	0.500	0.015(14)	0.000	0.000	0.500	0.007(11)
O2	0.260(6)	0.240(6)	0.000	0.021(8)	0.259(6)	0.241(6)	0.000	0.024(8)
	a=*b*=5.5815(2) Å, *c*=3.9546(3)Å					*a*=*b*=5.5830(2)Å, *c*=3.9548(3) Å		
	V= 123.20(1) Å^3, R_{wp}=3.77, R_{bragg}=2.37					*V*= 123.27(1) Å^3, R_{wp}=3.73, R_{bragg}=2.38		
Space group: *P4/mbm*(310 K)					Space group: *P4/mbm*(330 K)			
Atoms	*x*	*y*	*z*	U_{eq}(Å^2)	*x*	*y*	*z*	U_{eq}(Å^2)
Na/Ba/Ca	0.000	0.500	0.500	0.0105(7)	0.000	0.500	0.500	0.0105(7)
Nb/Ti	0.000	0.000	0.000	0.0089(5)	0.000	0.000	0.000	0.0088(4)
O1	0.000	0.000	0.500	0.006(11)	0.000	0.000	0.500	0.007(12)
O2	0.259(7)	0.241(7)	0.000	0.025(8)	0.258(8)	0.242(8)	0.000	0.026(9)
	a=*b*=5.5843(2)Å, *c*=3.9551(3)Å					*a*=*b*=5.5855(3)Å, *c*=3.9555(4)Å		
	V= 123.34(1) Å^3, R_{wp}=3.68, R_{bragg}=2.24					*V*= 123.40(1) Å^3, R_{wp}= 3.75, R_{bragg}=2.21		
Space group: *P4/mbm*(350 K)					Space group: *P4/mbm*(370 K)			
Atoms	*x*	*y*	*z*	U_{eq}(Å^2)	*x*	*y*	*z*	U_{eq}(Å^2)
Na/Ba/Ca	0.000	0.500	0.500	0.0108(7)	0.000	0.500	0.500	0.0089(6)
Nb/Ti	0.000	0.000	0.000	0.0088(4)	0.000	0.000	0.000	0.0090(3)
O1	0.000	0.000	0.500	0.006(4)	0.000	0.000	0.500	0.01(2)
O2	0.255(15)	0.245(15)	0.000	0.024(9)	0.253(12)	0.247(12)	0.000	0.021(7)
	a=*b*=5.5869(3)Å, *c*=3.9560(4)Å					*a*=*b*=5.5884(3)Å, *c*=3.9564(4)Å		
	V= 123.48(1) Å^3, R_{wp}=3.78, R_{bragg}=2.22					*V*= 123.56(2) Å^3, R_{wp}=4.01, R_{bragg}=2.36		

Space group: $P4/mbm$ (at 390 K)				
Atoms	*x*	*y*	*z*	U_{iso}(Å^2)
Na/Ba/Ca	0.000	0.000	0.500	0.0090(7)
Ti/Nb	0.000	0.000	0.000	0.009(5)
O1	0.000	0.000	0.500	0.014(16)
O2	0.253(11)	0.247(11)	0.000	0.022(9)
	a=*b*=5.5897(3)Å, *c*=3.9570(5)Å			
	V=123.64(2) Å^3			
	Agreement factors: R_{wp}=4.33, R_{bragg}=3.00			

V-F freezing temperature (T_{VF}) in the present system exhibiting relaxor-like characteristics. Similar to lead-based relaxors, displaying an average cubic structure with rhombohedral clusters at short ranges (that transform into a long-range rhombohedral phase below the freezing temperature (T_{VF})), NN-25BCT exhibits an average centrosymmetric antiferrodistortive tetragonal structure (SG: *P4/mbm*) at room temperature with polar clusters. These polar clusters transform into a non-centrosymmetric tetragonal ferroelectric phase (SG: *P4bm*) upon cooling.

The structure of an ideal perovskite is cubic with $Pm\bar{3}m$ space group [18]. However, most of the perovskites exhibiting fascinating properties are distorted. There exist three different types of distortions: (i) distortion of BO_6 octahedra, (ii) cationic displacements

Table 5.3 Structural parameters, and agreement factors for NN-25BCT obtained from the Rietveld refinements of the Synchrotron X-ray diffraction pattern at various temperatures using $Pm\bar{3}m$ model.

Space group: $Pm\bar{3}m$(410 K)					Space group: $Pm\bar{3}m$(430 K)			
Atoms	x	y	z	U_{eq}(Å^2)	x	y	z	U_{eq}(Å^2)
Na/Ba/Ca	0.000	0.000	0.000	0.0103(7)	0.000	0.000	0.000	0.0129(7)
Nb/Ti	0.500	0.500	0.500	0.0069(4)	0.500	0.500	0.500	0.0096(5)
O	0.500	0.500	0.000	0.0149(18)	0.500	0.500	0.000	0.0182(19)
		a=3.9552(1) Å				a=3.9560(1) Å		
		V= 61.87 Å^3, R_{wp}=4.44, R_{bragg}=4.12				V= 61.91 Å^3, R_{wp}=3.27 , R_{bragg}= 1.94		
Space group: $Pm\bar{3}m$(450 K)					Space group: $Pm\bar{3}m$(470 K)			
Atoms	x	y	z	U_{eq}(Å^2)	x	y	z	U_{eq}(Å^2)
Na/Ba/Ca	0.000	0.000	0.000	0.0133(7)	0.000	0.000	0.000	0.0138(7)
Nb/Ti	0.500	0.500	0.500	0.0097(5)	0.500	0.500	0.500	0.0098(5)
O	0.500	0.500	0.000	0.0181(19)	0.500	0.500	0.000	0.0183(19)
		a=3.9568(1) Å				a=3.9576(1) Å		
		V= 61.95 Å^3, R_{wp}=3.22, R_{bragg}=2.11				V= 61.99 Å^3, R_{wp}=3.29, R_{bragg}=2.07		
Space group: $Pm\bar{3}m$(490 K)					Space group: $Pm\bar{3}m$(500 K)			
Atoms	x	y	z	U_{eq}(Å^2)	x	y	z	U_{eq}(Å^2)
Na/Ba/Ca	0.000	0.000	0.000	0.0142(8)	0.000	0.000	0.000	0.0145(8)
Nb/Ti	0.500	0.500	0.500	0.0099(5)	0.500	0.500	0.500	0.0100(5)
O	0.500	0.500	0.000	0.0184(19)	0.500	0.500	0.000	0.0186(19)
		a=3.9584(1) Å				a=3.9595(1) Å		
		V= 62.02 Å^3, R_{wp}=3.26, R_{bragg}=2.09				V= 62.07 Å^3, R_{wp}=2.87, R_{bragg}=2.04		

(parallel/antiparallel), and (iii) tilting of BO_6 octahedra with respect to each other [58, 59]. It is important to note that these distortions can occur independently or in combination with each other. Correlated identical displacements of B-site cations are responsible for ferroelectricity and are linked with the Γ (k=0,0,0) point of the cubic brillouin zone. On the other hand, in-phase and out-of-phase octahedral tilting result in cell multiplication and are linked with M (k=1/2,1/2,0) and R (k=1/2,1/2,1/2) points of cubic brillouin zone [58, 59]. The distortions present in the low-symmetry structures correspond to a mode(s) that are soft in the high-symmetry cubic structure [74, 75]. Further, these soft modes are associated with the irreducible representations of the parent space group [74, 75]. Symmetry mode analysis quantifies the contribution of different modes in the low-symmetry distorted structure. In the present work, the low-temperature phase of NN-25BCT is ferroelectric, having a tetragonal symmetry with the P4bm space group (tilt system: $a_0^0a_0^0c_+^+$). For quantifying the structural distortions, we used *AMPLIMODES* program available at the Bilbao Crystallographic server [74, 75]. As input for *AMPLIMODES*, we have used the high-symmetry cubic phase (SG: $Pm\bar{3}m$ & a_0= 3.95854 Å) as a reference(parent) structure

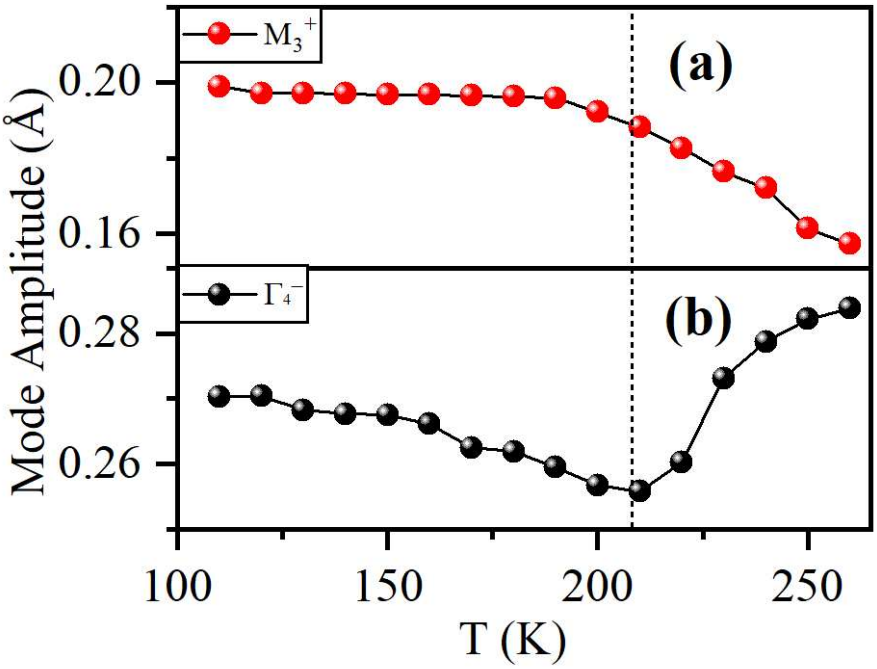

Fig. 5.4 Temperature-dependent evolution of (a) M_3^+ and (b) Γ_4^- modes in the stability region of long-range ferroelectric phase with *P4bm* space group calculated using the information obtained from refinement of SXRD patterns.

and the low-symmetry tetragonal (SG: *P4bm*) phase as a distorted structure. To describe the atomic positions of the undistorted cubic phase, we have used a Wyckoff sequence in which A, B, and O atoms occupy 1b (1/2,1/2,1/2), 1a (0,0,0), and 3d (1/2,0,0) sites, respectively. The transition from the cubic phase to the tetragonal phase occurs through the splitting of the Wyckoff sites(see Table 5.4). As indicated in Table 5.4, the two modes, Γ_4^- and M_3^+,

Table 5.4 Wyckoff site splitting in high- and low-symmetry structures with corresponding symmetry-breaking modes. Here, A and B represent the atoms positioned at the A and B sites of the perovskite structure.

Wyckoff site splitting		
SG: *Pm$\bar{3}$m*	**Symmetry breaking modes**	**SG: P4bm**
A 1b	Γ_4^-	A 2b
B 1a	Γ_4^-	B 2a
O 3d	Γ_4^-, M_3^+	O1 2a, O2 4c

are responsible for the symmetry-breaking transition $Pm\bar{3}m \rightarrow P4bm$. These irreducible

representations (irrep) *viz.*, M_3^+ and Γ_4^- are linked with the zone boundary and the zone centre of the cubic Brillouin zone, leading to in-phase rotations of adjacent octahedra and ferroelectric displacements in the unit cell, respectively. Therefore, we can quantify in-phase octahedral rotations and ferroelectric displacements by calculating the amplitudes of M_3^+ and Γ_4^- modes using *AMPLIMODES*. Now, the effect of octahedral rotations on ferroelectricity in the perovskite-based systems has been a matter of discussion for the last several decades [309, 310, 311, 312]. Generally, ferroelectricity (polar displacements) in perovskite-based systems increases with a decrease in temperature, and hence, the amplitude of the Γ_4^- phonon mode would increase with decreasing temperatures [313]. Fig. 5.4 illustrates the temperature-dependent evolution of the amplitude of Γ_4^- and M_3^+ modes. From 260 K to 220 K, the amplitude of M_3^+ mode increases and reaches its saturation value below 200 K. On the other hand, the amplitude of the Γ_4^- mode initially decreases up to 200 K, after which it increases with decreasing temperature. It is important to note that the amplitude of the Γ_4^- mode starts showing its obvious effect (i.e., increase in amplitude with the decrease in temperature) once the amplitude of M_3^+ mode reaches saturation. It is widely reported in the literature that octahedral tilts have detrimental effects on ferroelectricity for B-site driven ferroelectric materials [311, 312, 314, 315, 316], which can be observed as a reduction in the amplitude of the Γ_4^- mode. Thus, our experimental science results provide evidence for the competitive nature of octahedral tilts with ferroelectric displacements.

5.3.2 Short-range structural analysis

Fig. 5.5 shows polarization vs. electric field (P-E) and current vs. electric field (I-E) loops at a maximum field of 20 kV/cm and in ambient conditions. It is important to note that the slim hysteresis (P-E) loop and the switching peaks in the I-E curve suggest ferroelectric characteristics contrary to the long-range centrosymmetric structure with a tetragonal symmetry (SG: *P4/mbm*) at room temperature (i.e., 300 K). This ferroelectric response

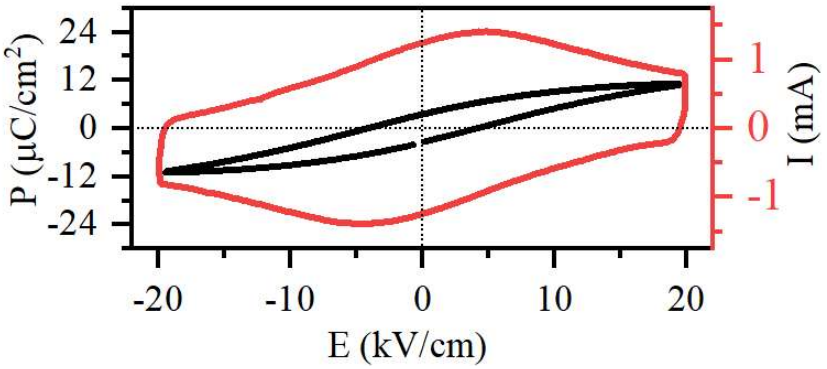

Fig. 5.5 Room temperature polarization vs electric field (P-E) and associated current vs electric field (I-E) loops of NN-25BCT measured at a maximum electric field of 20 kV/cm. The slim hysteresis loop is characteristic of a relaxor-like behaviour.

likely stems from the correlation among short-range ordered Polar nano regions typical of relaxors.

In order to explore short-range ordering and their symmetry, temperature-dependent Raman spectroscopy has been employed [71, 247, 248, 262]. We have collected the temperature-dependent Raman spectra in the temperature range $100 \leq T \leq 850$ K in the heating and cooling cycles (see Fig. 5.6; for clarity, only the heating cycle data are shown). It was observed that the spectral changes are fully reversible, without a temperature hysteresis within the experimental accuracy. All the Raman spectra were corrected for the Bose-Einstein population factor [317]. The Raman spectra can be decomposed into two distinct types of vibrational modes: (i) Motion of A-site cation with respect to BO_6 octahedra (external modes) and (ii) Isolated vibration of BO_6 octahedra, which involve bending and stretching modes (internal modes) [286]. At the lowest temperature (i.e., T = 100 K), there are three prominent broad peaks present around 250 cm^{-1}, 600 cm^{-1}, and 850 cm^{-1}. The Raman scattering near 250 cm^{-1} in the spectra of perovskite-type ferroelectric solid solutions is dominated by vibrations of off-centered B-site cations [318]. The Raman band near 600 cm^{-1} arises from BO_6 stretching modes, whereas the weak band near 800 cm^{-1} stems from a combination mode [169, 286, 319]. Significant Raman scattering was

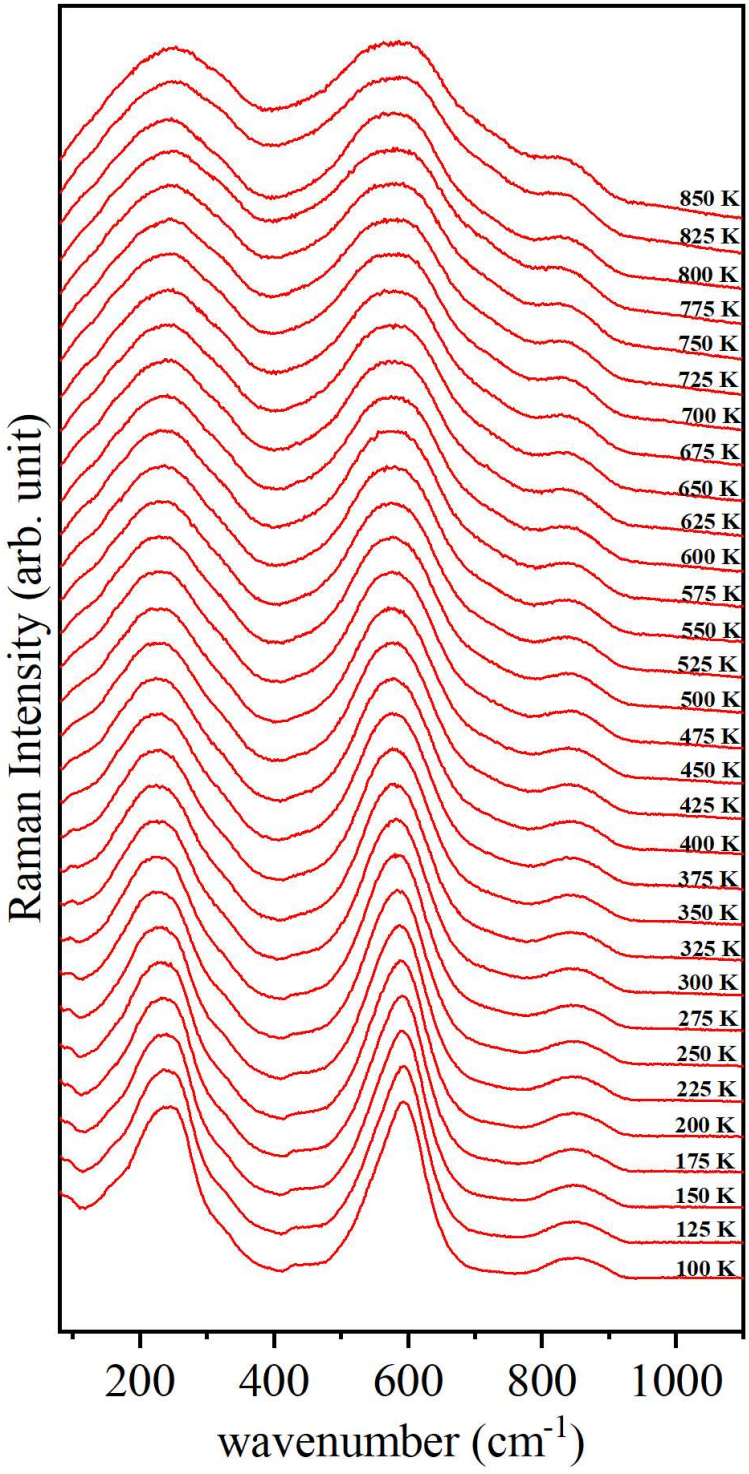

Fig. 5.6 Variable temperature Raman spectra of NN-25BCT in the temperature range 100 $\leq$ T $\leq$ 850 K. The Raman spectra have been taken during the heating cycle using the protocol described in the experimental section.

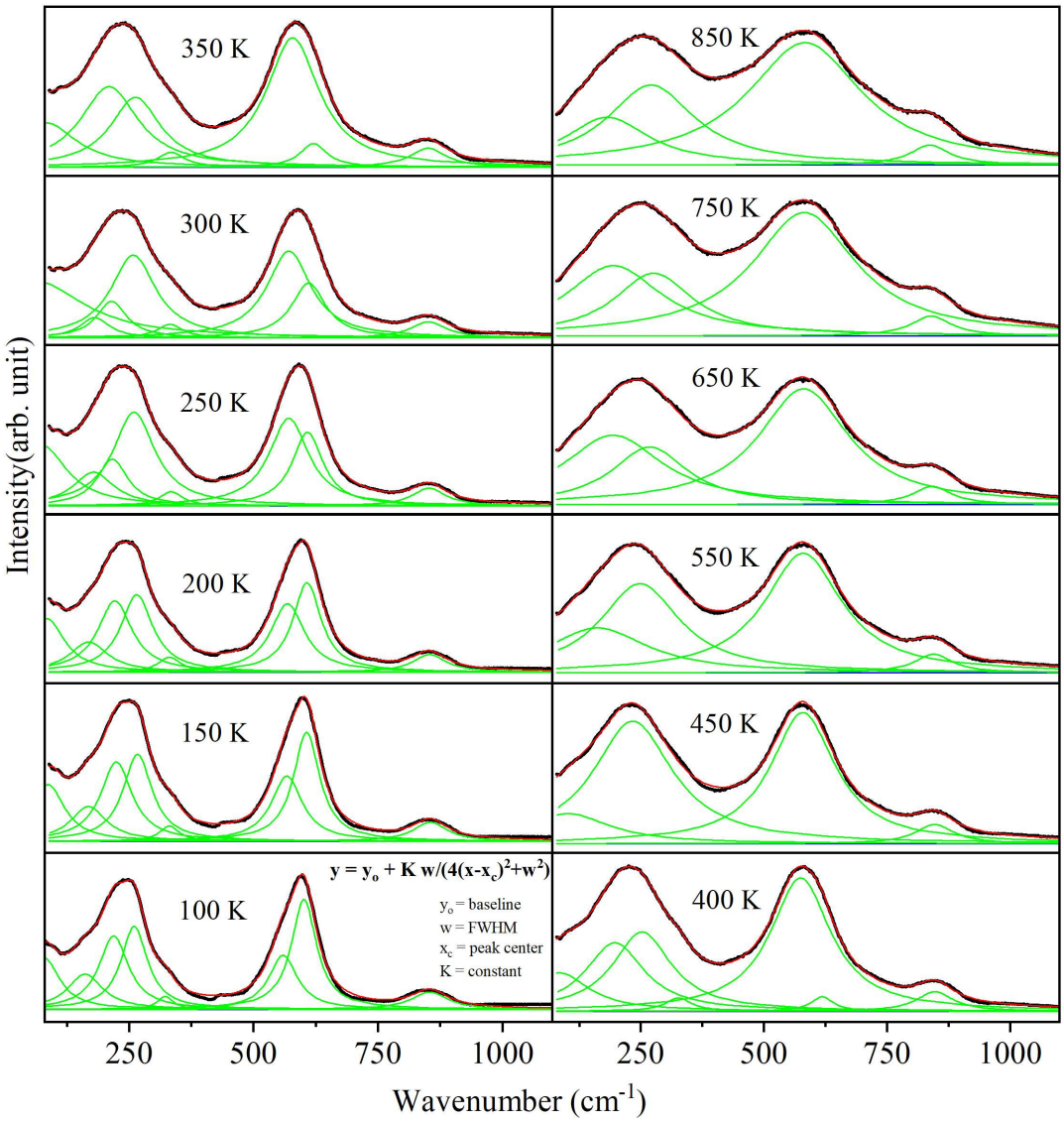

Fig. 5.7 Deconvoluted Raman spectra of NN-25BCT at some representative temperatures. All the Raman spectra have been fitted using a suitable number of Lorentz peaks.

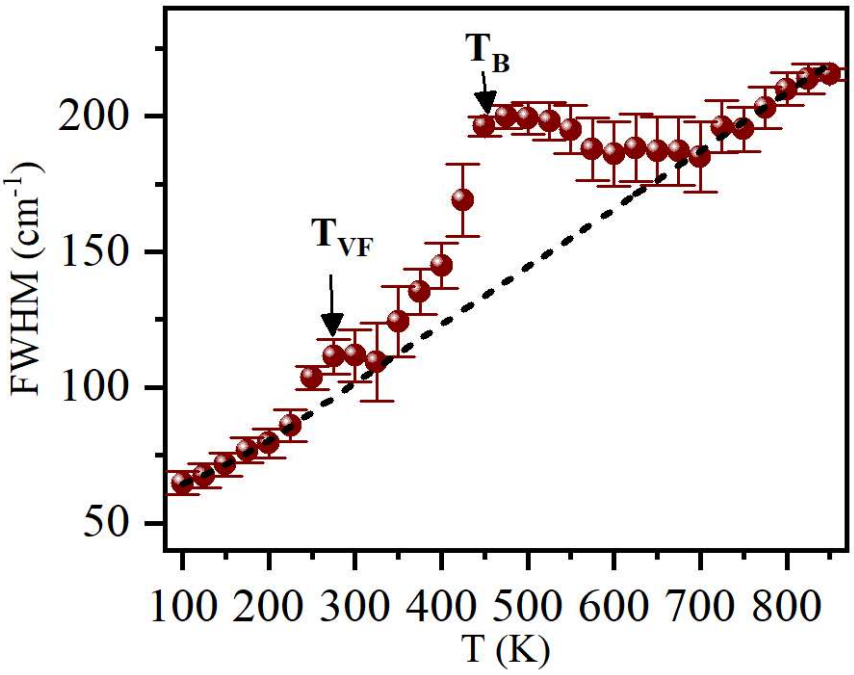

Fig. 5.8 Temperature-dependent variation of the FWHM of the Raman mode located near 250 cm^{-1}. The black dashed line is a polynomial baseline to account for the trivial decrease in phonon widths on heating.

detected above the Burns temperature (T_B), where the long-range structure is $Pm\bar{3}m$, with all atoms positioned at sites possessing a centre of inversion. As we know, first-order Raman scattering is prohibited for a centrosymmetric structure, and hence, such scattering is often attributed to cationic disorder or second-order effects [262, 286]. From the SXRD and dielectric analyses, it becomes evident that in NN-25BCT, a long-range polar phase exists only below the V-F freezing temperature T_{VF} ($\approx$ 270 K). Therefore, signatures of Raman modes at high temperatures offer strong evidence for the presence of ferroelectric ordering at short ranges (PNRs). Similar Raman spectra have also been reported earlier in related systems, where the ferroelectric ordering with tetragonal symmetry has been observed at short ranges [40, 119]. All the Raman spectra were fitted using a suitable number of Lorentz peaks (see Fig. 5.7). To shed light on the coupling processes between the B-site local dipoles, we have plotted the FWHM of the Raman scattering near 250 cm^{-1} against temperature (Fig. 5.8). It is clear that between 200 K and 700 K the data points

deviate from the trivial gradual increase of the phonon width with temperature (see the dashed line in Fig. 5.8), indicating ongoing local-scale rearrangements in the subsystem of off-centered B-site cations in the entire temperature range 200-700 K. The two maxima, near 270 and 420 K, mark the characteristic temperatures of structural transformations due to coupling of the B-site dipoles, which match very well T_{VF} and T_B derived from the temperature dependence of the dielectric permittivity (Fig. 5.1).

Generally, it has been observed in relaxors that the symmetry at long ranges is higher than the symmetry at short ranges (PNRs) [36, 320, 321, 322, 323, 324]. Pair distribution function (PDF) analysis is widely used for quantitative analysis of short-range structural distortions [325, 326]. Understanding such short-range structural distortions can provide insight into the relaxor-to-ferroelectric transition in NN-25BCT. In many relaxor systems, it has been observed that the long-range symmetry at low temperatures matches with the short-range symmetry (PNRs) at high temperatures in the non-polar phase [137, 138, 142, 307]. Fig. 5.9(a) shows the temperature-dependent atomic PDF profiles of NN-25BCT in a temperature range of $110 \leq T \leq 500$ K.

We do not see any significant changes in atomic PDF profiles on increasing temperature, except peak broadening indicative of increased thermal disorder at high temperatures. We have used the following plausible models to fit the experimental G(r) at 500 K; **(i)** ***Pm$\bar{3}$m*** **(cubic)**: corresponding to long-range symmetry at T > 400 K confirmed after Rietveld refinements **(ii)** ***P4/mbm*** **(tetragonal)**: corresponding to long-range symmetry of ergodic phase stable for $270 \leq T \leq 400$ K. **(iii)** ***P4bm*** **(tetragonal)**: corresponding to long-range symmetry stable for $110 \leq T \leq 260$ K. **(iv)** ***P4mm*** **(tetragonal)**: corresponding to long-range symmetry of $B_{0.9}C_{0.1}TiO_3$ (BCT) at room temperature [37, 327]. These models were inferred from the analysis of Synchrotron X-ray diffraction data in conjunction with literature [40, 119, 328]. Figure 5.9 (b) - (e) depicts PDF fits of different models with goodness of fit parameter (R_w).

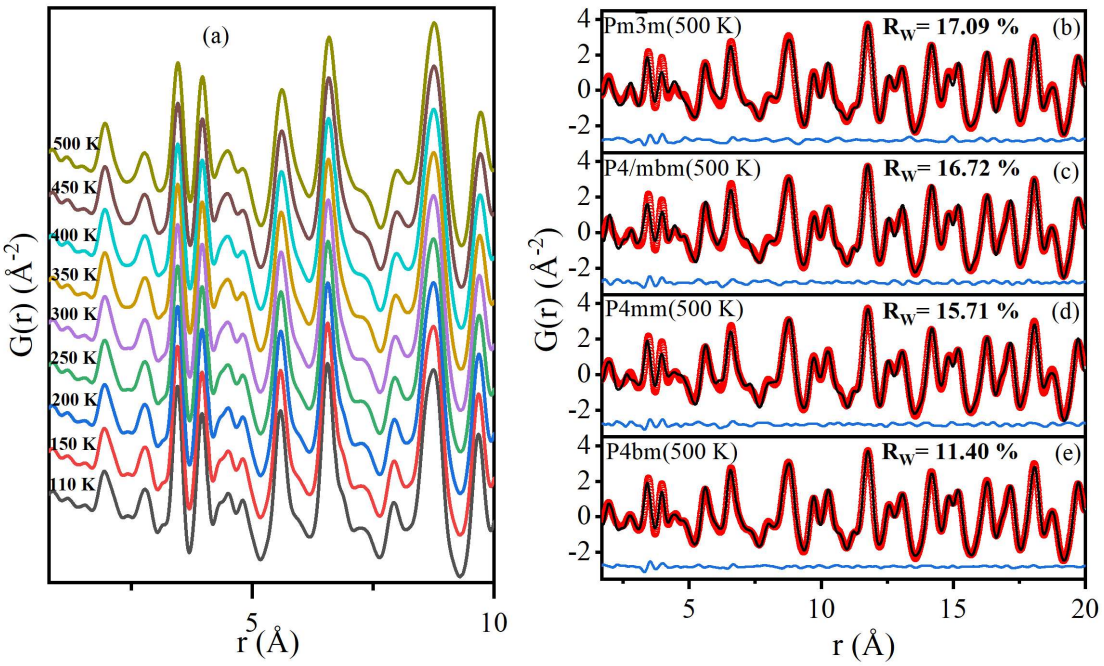

Fig. 5.9 (a) Temperature dependent evolution of PDF profiles of NN-25BCT. Atomic PDF fitting at 500 K using different plausible models *viz.,* (b) $Pm\bar{3}m$(c) *P4/mbm*, (d) *P4mm*, (e) *P4bm*. The goodness of fit parameter suggests that the *P4bm* model produces the best fit to the data.

We see that the tetragonal P4bm model provides the best fit with the lowest value of R_w. Therefore, we can conclude that the short-range structure at 500 K is polar with tetragonal symmetry (space group: *P4bm*) similar to what has been observed in Barium Titanate where long-range rhombhohedral(polar) symmetry of low temperatures is stable at short ranges in the high temperature paraelectric phase with cubic symmetry (space group: $Pm\bar{3}m$) [179]. Further, lowest R_w was achieved with *P4bm* model for all the PDF patterns (i.e., at all the temperatures). Moreover, wee see that the tetragonal phase at short ranges (space group: *P4bm*) is same as the low temperature phase of NN-25BCT stable at long ranges (concluded from SRXD analysis). Fig. 5.10 depicts the temperature-dependent fittings of experimental G(r) at some representative temperatures within the spatial range $1.7 \leq r \leq 20$ Å. To quantify the ferroelectric content at short ranges, symmetry mode analysis was performed using atomic coordinates and lattice parameters obtained from

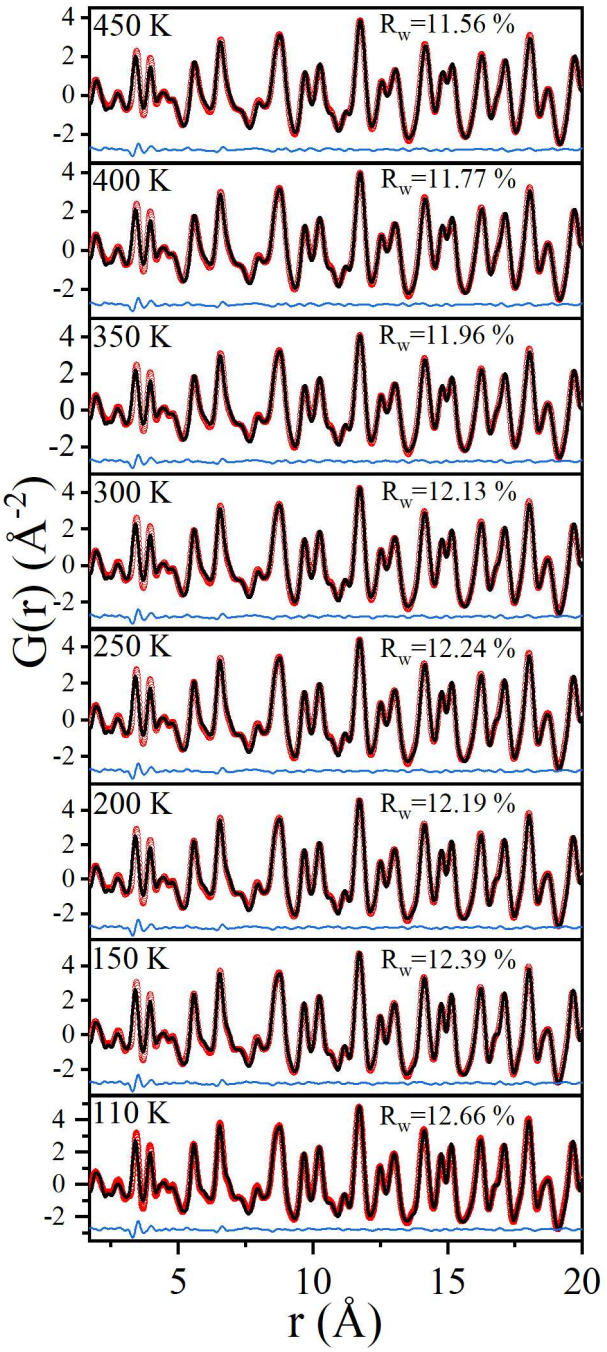

Fig. 5.10 The experimental (red dots) and calculated (black continuous line) pair distribution functions (PDFs) and their difference (blue line at the bottom) using the tetragonal space group (P4bm) in the temperature range 110 - 450 K obtained by refinement using the PDFgui program.

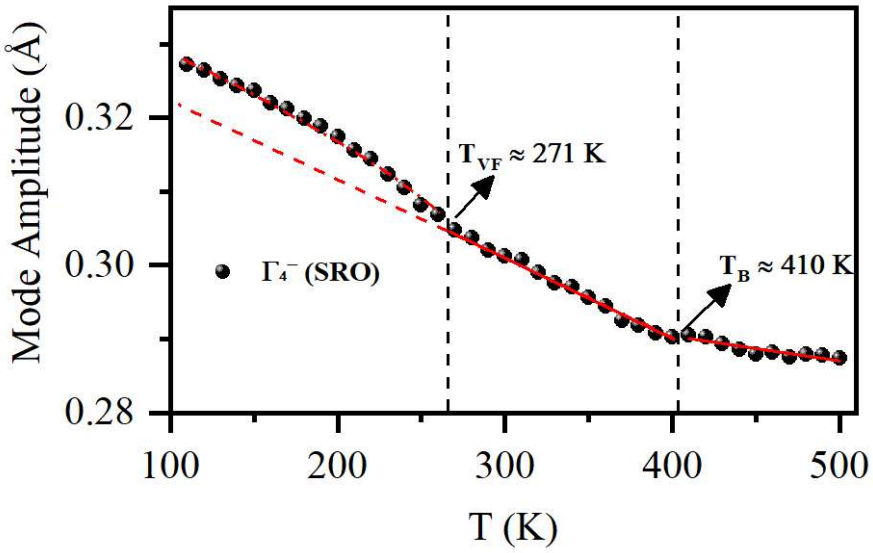

Fig. 5.11 Temperature dependent evolution of Γ_4^- mode calculated for short-range ordering(SRO) using the information obtained from refinement of PDF patterns.

the PDF refinements. As discussed earlier, the ferroelectric content of the short-range ordered (SRO) tetragonal phase (space group: *P4bm*) can be quantified using the amplitude of the ferroelectric phonon mode (Γ_4^-). Fig. 5.11 depicts the evolution of the amplitude of the Γ_4^- (SRO) mode as a function of temperature. The anomalies observed in the temperature-dependent evolution in the amplitude of the ferroelectric phonon mode at critical temperatures *viz.,* T_B and T_{VF} corroborate our conclusions inferred from the combined analysis of temperature-dependent dielectric, SXRD, and Raman spectroscopic data. The analysis of experimental PDF reveals that the ferroelectric displacements compatible with antiferrodistorted tetragonal symmetry (space group: *P4bm*) are present in the temperature range $110 \leq T \leq 500$ K. Due to a decrease in thermal disorder on lowering temperatures, the correlated ferroelectric displacements at short ranges form polar nano regions (characteristic of relaxors) below Burns temperature ($T_B \approx 410$ K), and eventually transform into a long-range ferroelectrically ordered state below Vogel-Fulcher freezing temperature ($T_{VF} \approx 270$ K). Moreover, we also notice that the short-range symmetry at high temperatures is the same as the long-range symmetry at low temperatures (i.e., tetragonal

with *P4bm* space group). This phenomenon is similar to what has been observed earlier for Barium Titanate and Sodium Niobate [36, 179]. Therefore, relaxor-to-ferroelectric transition in NN-25BCT can be attributed to the enhancement in correlations among PNRs on decreasing temperatures [138, 141, 149, 301, 329].

5.4 Conclusion

In summary, the dielectric analysis of NN-25BCT reveals relaxor-like behaviour with a freezing temperature $T_{VF} \approx 270$ K. Further, SXRD confirms a long-range relaxor (SG: *P4/mbm*) to ferroelectric (SG: *P4bm*) phase transition at low temperatures ($T < T_{VF}$). Our experimental work clearly reveals that in-phase octahedral tilting suppresses ferroelectricity in the perovskite-based systems by exploring the temperature-dependent evolution of the two primary order parameters *viz*, Γ_4^- and M_3^+ obtained using atomic coordinates and lattice parameters extracted from Rietveld analysis. Temperature-dependent Raman spectra reveal the presence of local polar distortions for temperatures above T_{VF}, contrary to the long-range centrosymmetric structure obtained from SXRD. Further, in line with Raman analysis, PDF interpretation provides evidence of local distortions with ferroelectric tetragonal ordering (SG: *P4bm*) stable throughout the studied range, i.e., 110 K $\leq$ T $\leq$ 500 K. Therefore, it is reasonable to believe that the relaxor to ferroelectric phase transition originates from the nucleation and growth of short-range ordered polar tetragonal phase (PNRs with *P4bm* symmetry) present in a long-range centrosymmetric matrix (with *P4/mbm* space group). This system can be a potential candidate for applications in pyroelectric detectors, electrocaloric devices, multi-layered ceramic capacitors (MLCCs), etc.